ChemComm

Accepted Manuscript

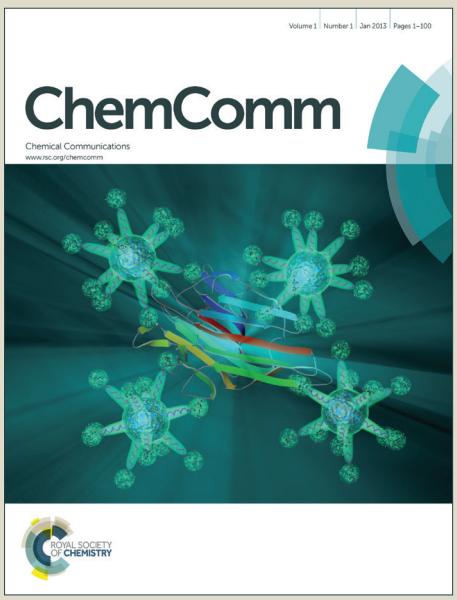

ROYAL SOCIETY OF CHEMISTRY

www.rsc.org/chemcomm

Journal Name

COMMUNICATION

Hydride Ion Formation in Stoichiometric UO_2

Received 00th January 20xx,
Accepted 00th January 20xx
DOI: 10.1039/x0xx00000x
www.rsc.org/

J.M. Flitcroft[a], M. Molinari[a], N. A. Brincat[a,b], M.T. Storr[b], S.C. Parker[a]

We investigated atomic hydrogen solubility in UO_2 using DFT. We predict that hydrogen energetically prefers to exist as a hydride ion rather than form a hydroxyl group by 0.27eV, and that on diffusion hydrogen's charge state will change. The activation energy for conversion of hydride to hydroxyl is 0.94eV.

UO_2 is the most widely used fuel in the nuclear industry. UO_2 readily oxidises by inclusion of interstitial oxygen, to form higher oxides, fluorite based U_4O_9, U_3O_7 and U_2O_5[1,2], and layered U_3O_8[3] and UO_3[4]. Oxidation of UO_2 is not limited to oxygen, but it involves fission products and hydrogen species, which greatly affect the fuel stability. During the fuel cycle, the material is exposed to hydrogen from the sintering process to the storage in the cooling ponds, where water leads to oxidative dissolution and hydrogen generation[5]. Dissolution also causes the release of radioactive isotopes stored within the fuel matrix.

However, despite the ubiquitous nature of hydrogen, there is limited research on hydrogen species in UO_2. Sherman and Olander[6] suggested that hydrogen dissolution in UO_2 occurs as monatomic species, although the nature of the dissolved species remains unknown. Hydrogen solubility was measured to be dependent on the stoichiometry and the crystalline nature of the sample[6-8], with hyperstoichiometric and stoichiometric UO_2 showing comparable solubility and hypostoichiometric UO_2 showing an order of magnitude increases in hydrogen solubility.

Computational work on hydrogen species in actinide oxides is scarce due to its quantum nature and the strong *f*-electron correlation in actinides, and limited to water interaction with UO_2 surfaces[9-11]. However, hydrogen in other materials has been studied[12, 13], and the nature of the hydrogen species, whether it is radical, hydride or proton, can be determined by using computational methodologies, thus unravelling the different charge states during dissolution and diffusion of hydrogen in the material.

In this communication, we present our work towards understanding the defect chemistry of hydrogen in stoichiometric UO_2, by studying the solubility of hydrogen in the lattice. However, before describing our findings we detail the methodology used.

The structural models were generated using the METADISE[14] code. A cubic unit cell comprised of 32 UO_2 units was generated by a 2 x 2 x 2 expansion of the fluorite unit cell (Fig. 1a), and an orthorhombic unit cell comprised of 12 UO_2 units was generated by re-orientating the fluorite lattice in the <111> direction (Fig. 1b). All calculations were performed using the VASP code[15], with PAW pseudo-potentials, the GGA and PBE +U functional[16]. The Dudarev[18] approach was used for the implementation of the onsite Hubbard U parameter, with U = 4.5eV and J = 0.54eV[19]. The plane-wave cut-off energy was 500eV for the 36 atom cell and 400eV for the 96 atom cell calculations. A 4 x 4 x 4 *k*-point mesh was used for the 36 atom cell and a 2 x 2 x 2 for the 96 atom supercell, resulting in *k*-point densities of 0.07Å^{-3} and 0.006Å^{-3}, respectively. Convergence criteria for the electronic and ionic relaxations were 1 x10^{-6} eV/atom and 0.01 eV/Å, respectively, and all calculations were performed at constant pressure with collinear 1*k* antiferromagnetic ordering. This is considered a good approximation for the experimentally observed 3*k* noncollinear antiferromagnetic (AFM) ordering[20, 21] and this methodology has been successfully used previously[21-23]. Isolated hydrogen defects were studied in the cubic unit cell by placing atomic hydrogen at the interstitial octahedral site and approximately 1Å from the oxygen lattice site (Fig. 1), the electrons are then relaxed to determine hydrogen species and compensating defects. The solution energy of hydrogen was calculated by subtracting the sum of the calculated energies for pure stoichiometric nUO_2 and ½H_2, from the calculated energy of the defective system $(UO_2)_nH$ following Equation 1.

$$nUO_{2(s)} + {}^1/_2 H_{2(g)} \rightarrow (UO_2)_n H_{(s)} \qquad \text{(Eq. 1)}$$

Following Sherman and Olander's work, we have calculated the solubility of monatomic hydrogen species in different locations and evaluated the energy barrier associated with the dissociation of hydrogen from a lattice oxygen atom to the octahedral interstitial site. In this case, we used the orthorhombic unit cell, where the hydrogen of the hydroxyl group is aligned along the diagonal of the oxygen cube (the <111> direction in the cubic cell in Fig. 1). We performed a series of calculations where the hydrogen was pulled from the hydroxyl group and at each step was allowed to relax in the plane perpendicular to the diagonal of the cube but not parallel to it.

The charge and magnetic states of all species and the associated defect energies were obtained as hydrogen was moved along this diffusion pathway. The pathway is depicted by an arrow in Fig. 1, where the equivalent start and end points for the hydrogen defects are shown in cubic and orthorhombic cells for comparison.

[a] Department of Chemistry, University of Bath, Claverton Down, Bath, Avon, BA2 7AY, UK
[b] AWE, Aldermaston, Reading, Berkshire RG7 4PR, UK
DOI: 10.1039/x0xx00000x

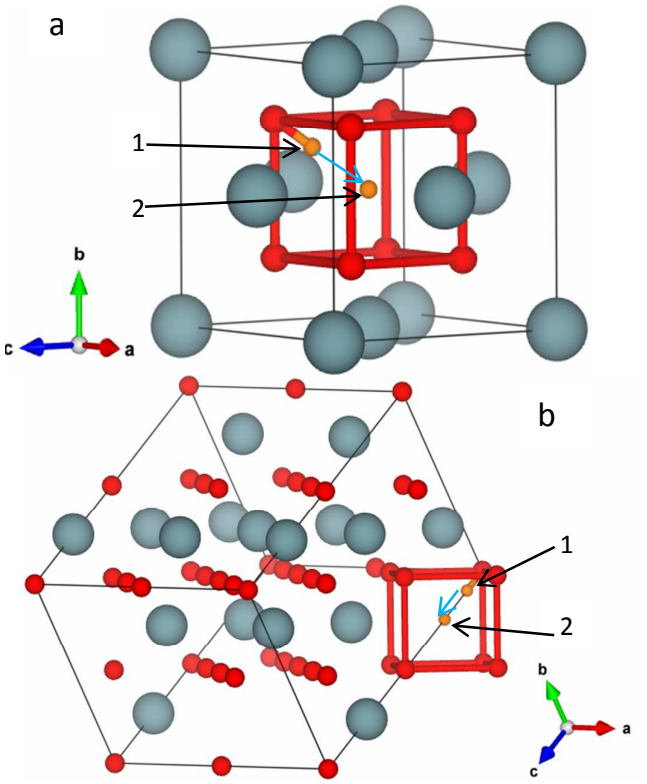

Fig. 1 Cubic (a) and orthorhombic (b) cells showing the hydroxyl hydrogen (1) and the hydride (2). The hydrogen atoms are in equivalent positions in both cell. Red atoms are oxygen, blue are uranium and orange are hydrogen. Bonds have been drawn on the oxygen sublattice for clarity. The hydroxyl hydrogen was pulled along the distance represented by the blue arrow as described in the text. Figures were created using VESTA[17].

Table 1 shows the calculated lattice parameters, angles and volume per uranium atom for the different simulation cells. For the 96 atom cell, the lattice parameters are double the experimental cubic unit cell parameters. There is a tetragonal distortion due to the stacking of the uranium layers with opposing magnetic moments (AFM ordering along <100> direction), which causes a small contraction along the magnetisation axis[23-25]. There is a small overestimation of the lattice parameters and unit cell volume compared with experiments, which has been reported previously using the DFT +U methodology[23-25].

VASP accounts for relativistic effects through the application of scalar relativistic methods[26, 27] and spin orbit coupling (SOC). The use of SOC for UO_2 (1.54μ_B and -3.25μ_B spin and orbital components) is consistent with the previously reported calculations[21] using the all electron code WIEN2K (1.80μ_B and -3.55μ_B spin and orbital components). However, SOC is not normally included because of the high computational overhead coupled with the results of previous work that has shown the effect of SOC to be negligible on structure, relative stability and electronic properties for the actinide dioxides[28]. Indeed, this is reproduced for the orthorhombic cell, where we compare the simulated cell dimensions with and without SOC in Table 1.

The results of adding atomic hydrogen are given in Table 2, which shows the final hydrogen species, solution energy and change in volume for the orthorhombic and cubic unit cells. We predict that hydrogen placed at the centre will be slightly offset from the interstitial octahedral site, becoming a hydride species compensated by the oxidation of a lattice U^{4+} to U^{5+}. The results show that the solution energies are strongly dependent on the defect concentration for the simulation cells we used, in large part due to the strain introduced as the uranium changes its oxidation state. This strain is exemplified by the defect volume of the hydrogen defect, reducing the volume by approximately 3Å^3 per hydrogen atom for hydride ion formation while increasing it by 7Å^3 per hydrogen for the hydroxyl. However, the difference in energy between the formation of a hydride and a hydroxyl, ΔE_f, is similar, 0.25eV for the orthorhombic unit cell with a concentration of 311μgH/gUO_2, compared to 0.27eV in the cubic unit cell with a concentration of 38.9μgH/gUO_2. The effect of including SOC is also shown in Table 2 for the orthorhombic cell, which results in a constant shift of the solution energies but it does not significantly alter the relative stability of the hydride.

Table 1 Comparison of calculated and experimental lattice parameters for the orthorhombic and cubic unit cells. The lattice parameters (a, b, c) are listed in Å, angles (α, β, γ) in degrees and volume (V) per U atom in Å^3.

Lattice Parameters	Ortho	Ortho (SOC)	Cubic	Exp[29] (Cubic)	Exp (Ortho)
a	7.87	7.83	10.93	5.47	7.72
b	6.76	6.80	11.05	5.47	6.69
c	9.60	9.56	11.05	5.47	9.46
α	89.35	89.98	89.99	90.00	90.00
β	89.99	90.01	89.99	90.00	90.00
γ	90.00	89.98	89.99	90.00	90.00
V per U atom	42.62	42.64	41.71	40.88	40.71

Table 2. Solution energies (E_f in eV) for 1 H atom in the orthorhombic and cubic cells. The hydrogen concentration in the simulation cell is [H] in μgH/gUO_2, ΔE_f is the difference in energy between the hydroxyl and hydride defect. The defect volume (V_{def} in Å^3) is the difference in volume between the defective and stoichiometric unit cells.

Cell	[H]	Defect Clusters	E_f	ΔE_f	V_{def}
Ortho	311	H^- / U^{5+}	1.31	–	-3.3
Ortho	311	OH / U^{3+}	1.56	0.25	7.2
Ortho (SOC)	311	H^- / U^{5+}	2.08	–	-2.8
Ortho (SOC)	311	OH / U^{3+}	2.30	0.22	7.8
Cubic	38.9	H^- / U^{5+}	0.20	–	-2.5
Cubic	38.9	OH / U^{3+}	0.47	0.27	7.3

In the case of the hydride, the compensating cation is not part of the uranium octahedral cage surrounding the hydrogen defect, and can therefore be thought of as residing in the next nearest neighbour position. Conversely, when the hydrogen atom was placed close to lattice oxygen, it formed a hydroxyl group compensated by the reduction of a lattice U^{4+} to U^{3+}, which is always at a nearest neighbour uranium site.

The electronic implications of these defects can be seen in Fig. 2, which shows the calculated partial density of states for stoichiometric UO_2, as well as UO_2 with hydride and hydroxyl defects in the cubic unit cell. The hydride is seen to occupy states just below the top of the valence band, while the U^{5+} states are at the bottom of the conduction band. For the hydroxyl defect the U^{3+} is now the top of the valence band.

A further intriguing result is that the hydrogen positions, when in the hydroxyl group or as a hydride ion, is comparatively close, less than 2Å. Hence, we calculated the relative solution energy of a hydrogen species and the accompanying change in volume of the orthorhombic unit cell as a single hydrogen atom moves along the path between the hydroxyl and hydride defect sites in the <111> cubic direction (Fig. 1b) and is given in Fig 3.

There are three distinct regions shown in Fig. 3. The first occurs close to the oxygen atom, up to 1.13Å, where the hydrogen is a proton, as part of a hydroxyl group, and there is a corresponding U^{3+} defect formed. This has a large increase (6.1Å^3 – 8.7Å^3) in the unit cell volume due to the formation of U^{3+}. The second region, between 1.13Å - 2.00Å from the oxygen atom, is where there is no change in oxidation state of the hydrogen or uranium. In this region the hydrogen is a radical and could be seen as an intermediate state between the hydride and proton species. This region is higher in energy and shows a small volume expansion (3.3Å^3– -0.2Å^3) compared to the stoichiometric unit cell. The final region, when the oxygen hydrogen distance is greater than 2.00Å, the final hydrogen species is a hydride and this is the most stable hydrogen defect. The formation of the hydride is accompanied by the formation of a U^{5+} and the shorter U^{5+}–O^{2-} distance, 2.31Å average, results in a decrease (-1.4Å^3 – -3.3Å^3) in unit cell volume. For the hydride defects, the U^{5+} formed as a next nearest neighbour defect (4.27Å - 5.85Å). The only two exceptions, where the U^{5+} defect formed as a nearest neighbour defect (2.36Å , 2.64Å), were both higher in energy than the positions to either side of them, however, the energy difference was only ~0.1eV. Thus whilst forming a U^{5+} as a nearest neighbour defect is less favourable, it is not accompanied by significant increase in energy.

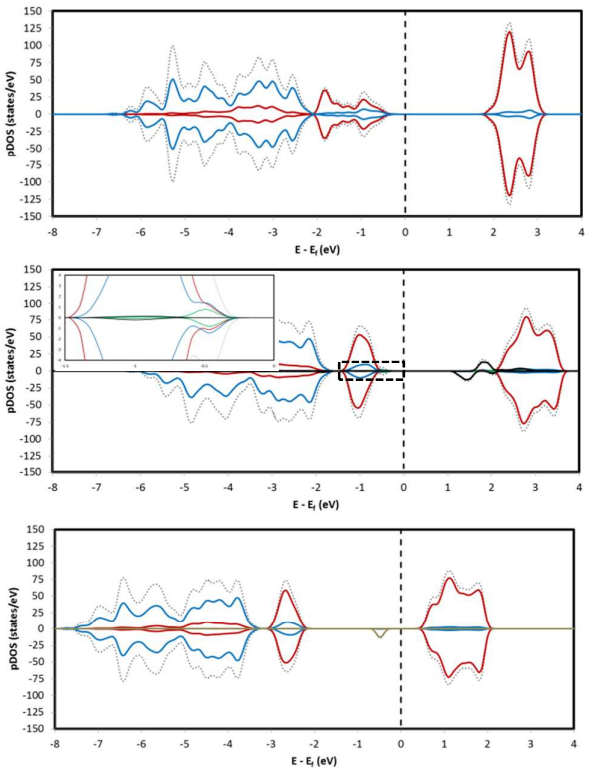

Fig 2. Partial density of states for pure UO_2 (top), hydride (middle) and hydroxyl (bottom) hydrogen defects in cubic unit cell. U^{3+} states shown in gold, U^{4+} in red, U^{5+} in black, H^- in green, O^{2-} in blue. The Fermi energy calculated using VASP has been set to zero. Evaluation of the hydroxyl states showed no states at the band gap so have been included in the oxygen states. Insert shows H^- states.

This suggests that there are multiple local minima, which may have implications for electron transport. As there are three distinct regions, shown in Fig. 3, where the hydrogen is a proton, then a

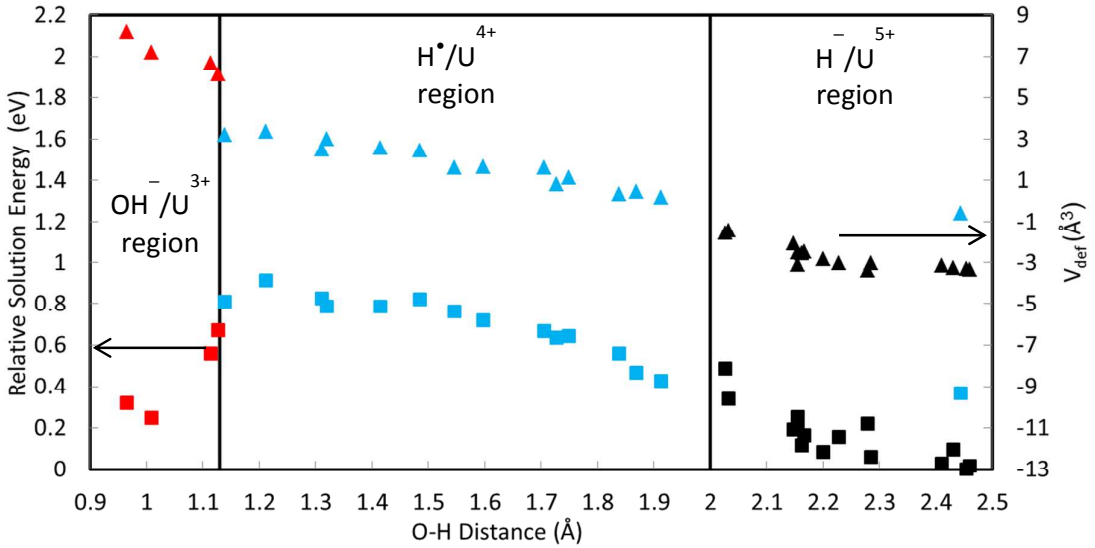

Fig. 3 The relative solution energy (Squares) and V_{def} (Triangles) for the hydrogen diffusion path in UO_2. Final hydrogen species represented by colour; red proton, blue radical and black hydride. The energies are set relative to the lowest energy configuration (H^- and U^{5+}).

radical and finally a hydride, this shows that the transition between the proton and hydride could occur as two one step processes, where the proton becomes a radical and then a hydride, rather than a single two step electron process where the proton becomes a hydride.

For all of the protonic defects, the corresponding U^{3+} is located at the nearest neighbour position (2.38Å – 3.56Å) and the larger U^{3+} ion with average U^{3+}–O^{2-} bond distances of 2.47Å results in cell expansion.

From Fig. 3, it is also possible to estimate the activation energy barrier for the formation a hydroxyl group from a hydride species; the barrier is 0.94eV. The presence of the two different defects, hydride and hydroxyl, relatively close to each other in location and with similar energies will have an influence on the diffusion of hydrogen in stoichiometric UO_2. It is possible that the diffusion of hydrogen could be a concerted mechanism involving both species, compared to the diffusion of hydrogen in CeO_2 where the hydrogen remains as a proton and moves as a proton from one lattice oxygen to the next[30]. It is therefore clear that the fluorite structure might trigger hydrogen dissolution but as the hydrogen solubility in CeO_2 was reported to be lower than in UO_2, this implies that the nature of the actinide cation impact significantly[6, 31]. Ce^{4+} does not oxidize to higher oxidation states while U^{4+} does[29], but readily reduces to Ce^{3+} while U^{4+} does not and hence, CeO_2, contrary to UO_2 is a mixed proton electron conductor as hydrogen dissolves as a proton forming hydroxyl groups[33, 34]. Thus, this work suggests that those metal oxides in which the metal more easily forms higher oxidation states may also support hydride formation. On the other hand, not least due to the quantum nature of hydrogen[35, 36], further work on the nature of the diffusing hydrogen speceis would be valuable.

In summary, stoichiometric UO_2 shows intricate hydrogen defect chemistry. The hydride is the most stable defect as it stabilizes the oxidation of U^{4+} to U^{5+}. However, the hydroxyl group is only 0.27eV less stable and stabilizes the reduction of U^{4+} to U^{3+}. Hydrogen defects share the octahedral interstitial site within 2Å. The activation energy to form a hydroxyl group from a hydride species is 0.94eV.

Acknowledgements

This work made use of ARCHER, the UK's national HPC funded by EPSRC (EP/L000202) through the Material Chemistry Consortium, and Aquila, the University of Bath's HPC. We thank AWE, the University of Bath and EPSRC (EP/I03601X/1) for funding.

References

1. G. C. Allen and N. R. Holmes, *J. Nucl. Mater.*, 1995, **223**, 231.
2. N. A. Brincat, M. Molinari, S. C. Parker, G. C. Allen and M. T. Storr *J. Nucl. Mater.*, 2015, **456**, 329.
3. N. A. Brincat, S. C. Parker, M. Molinari, G. C. Allen and M. T. Storr, *Dalton Trans.*,2015, **44**, 2613.
4. N. A. Brincat, S. C. Parker, M. Molinari, G. C. Allen and M. T. Storr, *Inorg. Chem.*, 2014, **53**, 12253.
5. H. He, M. Broczkowski, K. O'Neil, D. Ofori, O. Semenikhin and D. Shoesmith, 2012, NWMO TR-2012-09.
6. D. F. Sherman and D. R. Olander, *J. Nucl. Mater.*, 1989, **166**, 307.
7. D. R. Olander, D. Sherman and M. Balooch, *J. Nucl. Mater.*, 1982, **107**, 31.
8. V. J. Wheeler, *J. Nucl. Mater.,* 1971, **40**, 189.
9. T. Bo, J.-H. Lan, C.-Z. Wang, Y.-L. Zhao, C.-H. He, Y.-J. Zhang, Z.-F. Chai and W.-Q. Shi, *J. Phys. Chem.*, 2014, **118**, 21935.
10. P. Maldonado, L. Z. Evins and P. M. Oppeneer, *J. Phys. Chem. C*, 2014, **118**, 8491.
11. X.-f. Tian, H. Wang, H.-x. Xiao and T. Gao, *J. Nuc. Mater.*, 2014, **91**, 364.
12. E. L. da Silva, A. G. Marinopoulos, R. C. Vilao, R. B. L. Vieira, A. H.V., J. Piroto Duarte and J. M. Gil, *Phys. Rev. B*, 2012, **85**, 165211.
13. T. Norby, M. Wideroe, R. Glockner and Y. Larring, *Dalton Trans.*, 2004, 3012.
14. G. W. Watson, E. T. Kelsey, N. H. deLeeuw, D. J. Harris and S. C. Parker, *J. Chem. Soc., Faraday Trans.*, 1996, **92**, 433.
15. G. Kresse and J. Furthmuller, *Phys. Rev. B*, 1996, **54**, 11169.
16. J. P. Perdew, K. Burke and M. Ernzerhof, *Phys. Rev. Lett*, 1996, **77**, 3865.
17. K. Momma, F. Izumi, *J. Appl. Crystallogr.* 2008, **41**, 653-658.
18. M. R. Castell, S. L. Dudarev, C. Muggelberg, A. P. Sutton, G. A. D. Briggs and D. T. Goddard, *J. Vac. Sci. Techno. A*, 1998, **16**, 1055.
19. T. Yamazaki and A. Kotani, *J. Physl Soc. Jpn.*, 1991, **60**, 49.
20. B. Dorado, G. Jomard, M. Freyss and M. Bertolus, *Phys. Rev. B*, 2010, **82**, 035114-1.
21. R. Laskowski, G. K. H. Madsen, P. Blaha and K. Schwarz, *Phys. Rev.B*, 2004, **69**, 140408-1.
22. D. A. Andersson, J. Lezama, B. P. Uberuaga, C. Deo and S. D. Conradson, *Phys. Rev.B*, 2009, **79**, 024110-1.
23. M. Sanati, R. C. Albers, T. Lookman and A. Saxena, *Phys. Rev.B*, 2011, **84**, 014116-1.
24. D. Gryaznov, E. Heifets and E. Kotomin, *PCCP*, 2009, **11**, 7241.
25. B. Dorado, M. Freyss and G. Martin, *EPJB*, 2009, **69**, 209.
26. L. Kleinman, *Phys. Rev. B*, 1980, **21**.
27. A. H. MacDonald, W. E. Pickett and D. D. Koelling, *J.Phys. Chem. C: Solid State Physics*, 1980, **13**.
28. X.-D. Wen, R. L. Martin, L. E. Roy, G. E. Scuseria, S. P. Rudin, E. R. Batista, T. M. McCleskey, B. L. Scott, E. Bauer, J. J. Joyce and T. Durakiewicz, *J. Chem. Phys.*, 2012, **137**.
29. L. Desgranges, G. Baldinozzi, G. Rousseau, J. C. Niepce and G. Calvarin, *Inorg. Chem.*, 2009, **48**, 7585.
30. Y. Nigara, K. Kawamura, R.Kawada, J. Mizusaki, M. Ishigame, *J. Eletrochem. Soc.*, 1999, **146**, 2948.
31. N. Sakai, K. Yamaji, H. Terushia, H. Yokohawa, Y. Hirata, S. Sameshima, Y. Nigara and J. Mizusaki, *Solid State Ionics*, 1999, **125**, 325.
32. K. O. Kvashnina, S. M. Butorin, P. Martin and P. Glatzel, *Phys. Rev. Lett.*, 2013, **111**, 253002-1.
33. M. Molinari, S. C. Parker, D. C. Sayle and M. S. Islam, *J. Phys. Chem. C*, 2012, **116**, 7073.
34. D. R. Mullins, P. M. Albrecht, T.-L. Chen, F. C. Calaza, M. D. Biegalski, H. M. Christen and S. H. Overbury, , *J. Phys. Chem. C*, 2012, **116**, 19419.
35. L. Xin-Zheng, B. Walker and A. Michaelides, *PNAS,* 2011, **108**, 6369.
36. M. Ceriotti, J. More and D. E. Manolopoulos, *Comput. Phys. Commun.*, 2014, **185**, 1019